RSC Advances

PAPER

View Article Online
View Journal | View Issue

Cite this: *RSC Adv.*, 2018, **8**, 36383

Cerium and tin oxides anchored onto reduced graphene oxide for selective catalytic reduction of NO with NH_3 at low temperatures

Yanli Wang,[a] Ying Kang,[a] Meng Ge,[a] Xiu Zhang[a] and Liang Zhan *[ab]

A series of cerium and tin oxides anchored on reduced graphene oxide (CeO_2–SnO_x/rGO) catalysts are synthesized using a hydrothermal method and their catalytic activities are investigated by selective catalytic reduction (SCR) of NO with NH_3 in the temperature range of 120–280 °C. The results indicate that the CeO_2–SnO_x/rGO catalyst shows high SCR activity and high selectivity to N_2 in the temperature range of 120–280 °C. The catalyst with a mass ratio of (Ce + Sn)/GO = 3.9 exhibits NO conversion of about 86% at 160 °C, above 97% NO conversion at temperatures of 200–280 °C and higher than 95% N_2 selectivity at 120–280 °C. In addition, the catalyst presents a certain SO_2 resistance. It is found that the highly dispersed CeO_2 nanoparticles are deposited on the surface of rGO nanosheets, because of the incorporation of Sn^{4+} into the lattice of CeO_2. The mesoporous structures of the CeO_2–SnO_x/rGO catalyst provides a large specific surface area and more active sites for facilitating the adsorption of reactant species, leading to high SCR activity. More importantly, the synergistic interaction between cerium and tin oxides is responsible for the excellent SCR activity, which results in a higher ratio of $Ce^{3+}/(Ce^{3+} + Ce^{4+})$, higher concentrations of surface chemisorbed oxygen and oxygen vacancies, more strong acid sites and stronger acid strength on the surface of the CeSn(3.9)/rGO catalyst.

Received 15th June 2018
Accepted 18th October 2018

DOI: 10.1039/c8ra05151h

rsc.li/rsc-advances

1. Introduction

Nitrogen oxides (NO_x) emitted from flue gases are considered to be one of the major air pollutants, and must be removed before emission. Selective catalytic reduction (SCR) of NO with NH_3 has become the mainstream strategy of industrial application and research due to its high NO_x removal efficiency and low energy consumption.[1,2] Up to now, commercial SCR catalysts (such as V_2O_5/TiO_2, V_2O_5–WO_3/TiO_2) must be operated in a high temperature range of 350–450 °C to avoid catalyst deactivation by SO_2,[3,4] while the stack gas temperatures in many industrial boilers are only about 120–250 °C. To satisfy the high reaction temperature (350–450 °C) for V_2O_5/TiO_2 based catalysts, existing boiler systems must be coupled with a heating system or the flue gases are preheated, resulting in high energy consumption. Therefore, various novel low temperature SCR catalysts are designed and developed for practical NO_x removal, such as V_2O_5, CeO_2, MnO_x, MnO_x–CeO_2 supported on TiO_2 (ref. 5–7) or carbon materials (activated carbon,[8] activated carbon fibers,[9] carbon nanotubes[10–12] and honeycomb activated carbon[13,14]).

Among the novel SCR catalyst candidates, MnO_x–CeO_2 catalysts have attracted much attention due to their high NO_x removal activities and resistance to SO_2 poisoning in the low temperature range of 100–200 °C.[15,16] The promoting effect of CeO_2 is attributed to its unique redox property and excellent oxygen storage capacity,[17,18] which associates with the formation of oxygen vacancies. As literatures reported,[7,18] the replacement of partial cerium atoms in the CeO_2 lattice by the other transition metal ions caused the distortion of CeO_2 lattice and generated defects, resulting in improved thermal stability and increased SCR activity. However, it should be pointed out that MnO_x–CeO_2 based catalysts exhibit low SCR activities especially in the presence of SO_2. To improve the resistance to SO_2 poisoning in NO removal, the MnO_x–CeO_2 catalysts modified with SnO_2 have been developed. Chang *et al.*[19,20] reported SnO_2-modified MnO_x–CeO_2 catalysts enhanced the SCR activity, broadened the operating temperature window (80–300 °C) and exhibited good SO_2 resistance. Our recent studies[21] revealed that spherical activated carbons supported SnO_x–CeO_2–MnO_x catalyst (SnCeMn/SACs) with a molar ratio of Sn/Mn = 0.25 yielded higher than 95% NO conversion in the temperature range of 140–280 °C, and showed high SO_2 resistance. At 240 °C, NO conversion over SnCeMn/SACs gradually decreased from 96% in the absence of SO_2 to about 77% in 480 min upon the

[a]*State Key Laboratory of Chemical Engineering, Key Laboratory for Specially Functional Polymers and Related Technology of Ministry of Education, Shanghai Key Laboratory of Multiphase Materials Chemical Engineering, East China University of Science and Technology, Shanghai 200237, China. E-mail: zhanliang@ecust.edu.cn; Fax: +86 21 64252914*

[b]*CAS Key Laboratory of Carbon Materials, Institute of Coal Chemistry, Chinese Academy of Sciences, Taiyuan 030001, China*

introduction of SO_2 in the feed gas. Recently, it has also been demonstrated CeO_2–SnO_x catalysts showed high SCR activities, which was attributed to the strong synergistic effect between Ce and Sn species, leading to increased surface acidity of Lewis acid sites.[22] Based on the high activities of CeO_2–SnO_x based catalysts, it is necessary the development of CeO_2–SnO_x in nanoscale to further improve their SCR activities. As a novel carbon nanomaterial, reduced graphene oxide (rGO) has been attracted attention, because of its unique two-dimensional microstructure and the existence of a certain amount of oxygen-containing functional groups on it.[23,24] Therefore, the combination of rGO nanosheets and CeO_2–SnO_x are expected to achieve nanostructured CeO_2–SnO_x that provides larger reaction interfaces, leading to the enhancement of the catalytic activity.

In this work, a series of CeO_2–SnO_x anchoredon reduced grapheme oxide (CeO_2–SnO_x/rGO) catalysts are synthesized using hydrothermal method and their activities for SCR of NO are evaluated. The effects of SnO_x on the activities, structures and surface properties of CeO_2/rGO catalyst are also investigated. The catalysts are characterized to understand the physical and chemical properties of CeO_2–SnO_x/rGO as well as the relationship between structure and catalytic activity. The obtained CeO_2–SnO_x/rGO catalysts exhibit high SCR activities in the low temperature range of 120–280 °C, resulted from the highly dispersed CeO_2 nanoparticles, mesoporous structures with high surface area and the synergistic interaction between cerium and tin oxides.

2. Experimental

2.1 Catalyst preparation

All the chemical reagents purchased from Aldrich were analytical grade. The graphene oxide (GO) was prepared using the modified Hummers.[25] The CeO_2–SnO_x/rGO catalysts were synthesized by the hydrothermal method using GO, $Ce(NO_3)_3 \cdot 6H_2O$ and $SnCl_4 \cdot 5H_2O$ as the precursors. In a typical procedure, 100 mg GO was initially dispersed in 50 mL deionized water by ultrasonic treatment for 3 h. Then appropriate amounts of $Ce(NO_3)_3 \cdot 6H_2O$ and $SnCl_4 \cdot 5H_2O$ were dropped slowly into the GO slurry and the mixture was stirred for 1 h. Subsequently, ammonia solution was added into the above solution under vigorously stirring until the pH value reached.[11] After stirring for 30 min, the obtained suspension was transferred into a 100 mL Teflon-lined stainless autoclave and heated at 180 °C for 12 h. Finally, the product was washed with deionized water and then freeze-dried for 24 h, followed by calcination at 300 °C for 2 h in N_2 atmosphere. The molar ratio of Sn/Ce in all CeO_2–SnO_x/rGO catalysts is controlled at 0.5, which was reported to be the optimum ratio of Ce–Sn/TiO_2 catalyst for NO removal.[26] Besides, the mass ratios of (Ce + Sn)/GO is 1.3, 2.6 and 3.9, respectively. The resultant catalysts are denoted as CeSn(*m*)/rGO, where *m* presents the mass ratio of (Ce + Sn)/GO. For example, CeSn(1.3)/rGO refers to the mass ratio of (Ce + Sn)/GO is 1.3 in the CeO_2–SnO_x/rGO catalyst. For comparison, CeO_2/rGO and SnO_x/rGO were also synthesized using the similar procedure.

2.2 Activity test

The activity test was carried out in a fixed-bed reactor with a diameter of 12 mm. At steady state, the feed gases are consisted with 500 ppm NO, 500 ppm NH_3, 5 vol% O_2, 200 ppm SO_2 (when used), and balance N_2. The total flow rate was controlled at 500 mL min^{-1}, where the gas hourly space velocity (GHSV) is 62 500 h^{-1}, and the reaction temperature was regulated from 120 to 280 °C. The concentrations of NO and O_2 in the inlet and outlet gases were continually monitored on-line by a flue gas analyzer (MRU VARIO PLUS, Germany). The effluent gas concentrations of NO and N_2O were monitored by Nicolet (FTIR, PROTÉGÉ460, America). The SCR behaviors of the catalysts are expressed by NO conversion and N_2 selectivity, which were calculated as literature reported.[27]

2.3 Characterization

Nitrogen adsorption/desorption isotherms of the samples were performed by Micromeritics ASAP 2020 M analyzer, and the pore size distributions were obtained by the Barrett–Joyner–Halenda (BJH) model. Raman and Fourier transform infrared (FT-IR) spectra were recorded on a Spex 1403Raman spectrometer and a Nicolet 5700 FTIR spectrometer, respectively. Powder X-ray diffraction (XRD) patterns of the samples were recorded by a Riguku D/Max 2550 diffractometer using Cu Kα radiation. The lattice parameters and crystallite sizes of all samples were calculated according to Bragg's law and the Debye–Scherrer equation, respectively. The microstructures of the samples were investigated using a JEOLJSM-6360LV scanning electron microscope (SEM) and a JEOL JEM-2010 transmission electron microscopy (TEM). The surface compositions of the catalysts were analyzed by X-ray photoelectron spectroscopy (XPS) with a PHI 5000 VersaProbe system. NH_3-temperature programmed desorption (NH_3-TPD) experiments were carried out on an adsorption apparatus (TP-5080, Xianquan Co.) with a thermal conductivity detector (TCD). 0.1 g sample was loaded into the reactor and pretreated at 300 °C for 30 min in He stream, and then cooled to 100 °C in He. Then the He flow was switched to a stream containing 5 vol% NH_3/He to adsorb NH_3 for 60 min at 100 °C. And subsequently the sample was purged with He at the same temperature. Finally, the sample was heated in He from 100 °C to 800 °C at a heating rate of 10 °C min^{-1}.

3. Results and discussion

3.1 SCR activities

Fig. 1 presents the SCR activities *versus* reaction temperature over the CeO_2/rGO, SnO_x/rGO and CeO_2–SnO_x/rGO catalysts. The CeO_2/rGO catalyst exhibits a relatively high SCR activity, and NO conversion increases from 34% at 120 °C to 68% at 180 °C, and is more than 83% from 200 to 280 °C. Although NO conversion of SnO_x/rGO catalystis less than 15% in the temperature range of 120–280 °C, interestingly, the CeSn(3.9)/rGO catalyst shows a higher SCR activity than both of CeO_2/rGO and SnO_x/rGO catalysts. NO conversion of the CeSn(3.9)/rGO catalyst can achieve about 86% at 160 °C, and above 97% at temperatures of 200–280 °C, respectively. These results

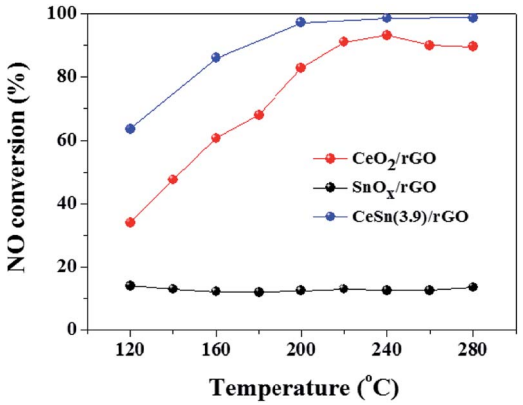

Fig. 1 NO conversions over various catalysts at different reaction temperatures.

indicate that the interaction between CeO_2 and SnO_x is beneficial to promote the SCR activity of CeO_2/rGO catalyst.

Since Fig. 1 indicates that the addition of SnOx has a positive effect on the SCR activity of CeO_2/rGO catalyst, the SCR activities of CeO_2–SnO_x/rGO catalysts with different mass ratios of (Ce + Sn)/GO were further investigated. As shown in Fig. 2a, all the CeO_2–SnO_x/rGO catalysts exhibit high SCR activities and NO conversions of all the catalysts increase with increasing reaction temperature. NO conversion of CeSn(1.3)/rGO catalyst is less than 30% in the low temperature range of 120–160 °C, and it reaches about 80% at 280 °C. Furthermore, NO conversion is obviously and greatly enhanced with increasing mass ratio of (Ce + Sn)/GO at different reaction temperatures. NO conversion of CeSn(2.6)/rGO catalyst can increase to about 91% at 200 °C, and about 98% at temperatures of 240–280 °C. NO conversion of CeSn(3.9)/rGO catalyst can reach about 64% at 120 °C, about 86% at 160 °C and about 97% at 200 °C. And it shows nearly 99% NO conversion in the temperature range of 240–280 °C. This SCR activity result is better than the data reported in the literatures for CeO_2–SnO_x (ref. 22), $CeO_2/Ti_xSn_{1-x}O_2$ (ref. 28) and H-CeSnTiO_x (ref. 29) catalysts in the temperature range of 120–280 °C. The increase in SCR activity with increasing mass ratio of (Ce + Sn)/GO may be attributed to the increase of active sites on the surface of catalyst. Fig. 2b shows the N_2 selectivity at different temperatures over CeSn(1.3)/rGO, CeSn(2.6)/rGO and CeSn(3.9)/rGO catalysts. The N_2 selectivity of all the catalysts decreases with increasing temperature, however, higher than 95% N_2 selectivity is still obtained at 280 °C. This result is similar to that reported on other CeO_2–SnO_x based catalysts.[22,28,29] Therefore, the CeSn(3.9)/rGO catalyst is very active and highly selective for the SCR of NO.

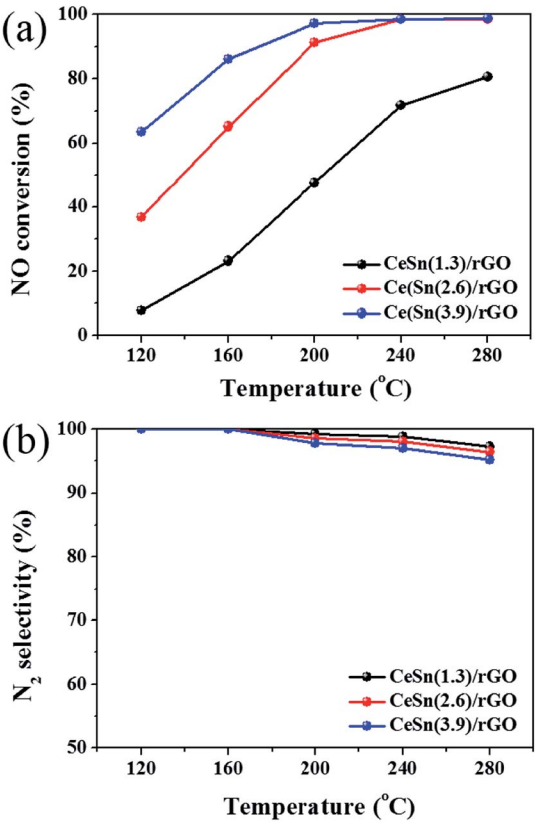

Fig. 2 NO conversions (a) and N_2 selectivity (b) over CeO_2–SnO_x/rGO catalysts with different mass ratios of (Ce + Sn)/GO.

3.2 Morphological and structural characterization of the catalysts

3.2.1 Morphology. The morphology and microstructure of the CeSn(3.9)/rGO catalyst are characterized using TEM. As shown in Fig. 3a, CeO_2 nanoparticles with the average size of about 6 nm are dispersed homogeneously on the rGO nanosheets, and the HRTEM image reveals that the visible lattice fringes with a lattice spacing of 0.31 and 0.26 nm, corresponding to the (111) and (220) crystal planes of CeO_2 (Fig. 3b). Compared with CeO_2/rGO, the size of metal oxides nanoparticles in the CeSn(3.9)/rGO significantly becomes smaller (Fig. 3c). The coexistence of cerium and tin oxides decreases the nanoparticle size, indicating that there exists strong interaction between CeO_2 and SnO_x.[30] Interestingly, although the (111) crystal plane of CeO_2 can be also clearly observed (Fig. 3d) on the CeSn(3.9)/rGO, the (110) crystal plane of SnO_2 with a lattice

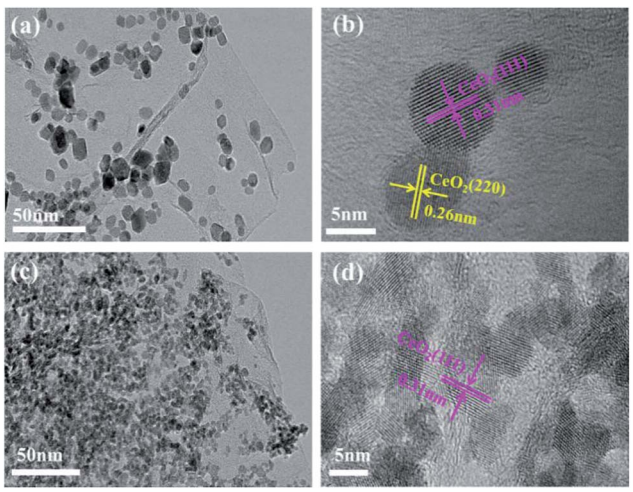

Fig. 3 TEM and HRTEM images of CeO_2/rGO (a and b) and the CeSn(3.9)/rGO catalyst (c and d).

spacing of 0.33 nm cannot be observed.[31] Therefore, the highly dispersed nanoparticles after the addition of SnO_x are expected to be favourable for the enhancement of the SCR activity.

3.2.2 Physical and chemical properties. The nitrogen adsorption/desorption isotherms of CeO_2/rGO and CeO_2–SnO_x/rGO catalysts exhibit typical type-IV curves with a hysteresis loop (Fig. 4a), suggesting that there exists mesoporous structures produced during the hydrothermal process. CeO_2/rGO has a specific surface area of 133.4 $m^2\ g^{-1}$ and an average pore size of about 8.43 nm (Table 1). The addition of SnO_x to CeO_2/rGO causes an increase in specific surface area, and the specific surface areas of CeSn(1.3)/rGO, CeSn(2.6)/rGO and CeSn(3.9)/rGO are 249.1, 220.8 and 197.7 $m^2\ g^{-1}$, respectively. The specific surface areas of these CeO_2–SnO_x/rGO catalysts are much larger than the data reported for CeO_2–SnO_x (63 $m^2\ g^{-1}$),[22] $CeO_2/Ti_xSn_{1-x}O_2$ (75.6 $m^2\ g^{-1}$)[28] and H-CeSnTiO_x (133.6 $m^2\ g^{-1}$),[29] which may be explained because rGO nanosheets can prevent the agglomeration of CeO_2 and SnO_x nanoparticles, agreeing with the TEM result. It is worth noting that the average pore size of CeO_2–SnO_x/rGO catalysts is much smaller than that of the CeO_2/rGO catalyst (Fig. 4b), suggesting the structural change of the catalysts to some extent. Therefore, it can be concluded that the mesoporous structures with larger specific surface area of CeO_2–SnO_x/rGO catalysts can provide more surface active sites for facilitating the adsorption of reactant species, leading to the increase in SCR activity.

To determine the total contents of CeO_2 and SnO_x in the CeO_2–SnO_x/rGO catalysts, TG were carried out from 25 to 800 °C in air atmosphere (Fig. 4c). From TG curves, a small weight loss below 150 °C is attributed to the removal of physically adsorbed water in the samples. And the obvious weight loss between 280 and 500 °C is ascribed to the combustion of grapheme into CO_2. The residual weight after TG tests is determined to be 67.0%, 78.9% and 84.4% for CeSn(1.3)/rGO, CeSn(2.6)/rGO and

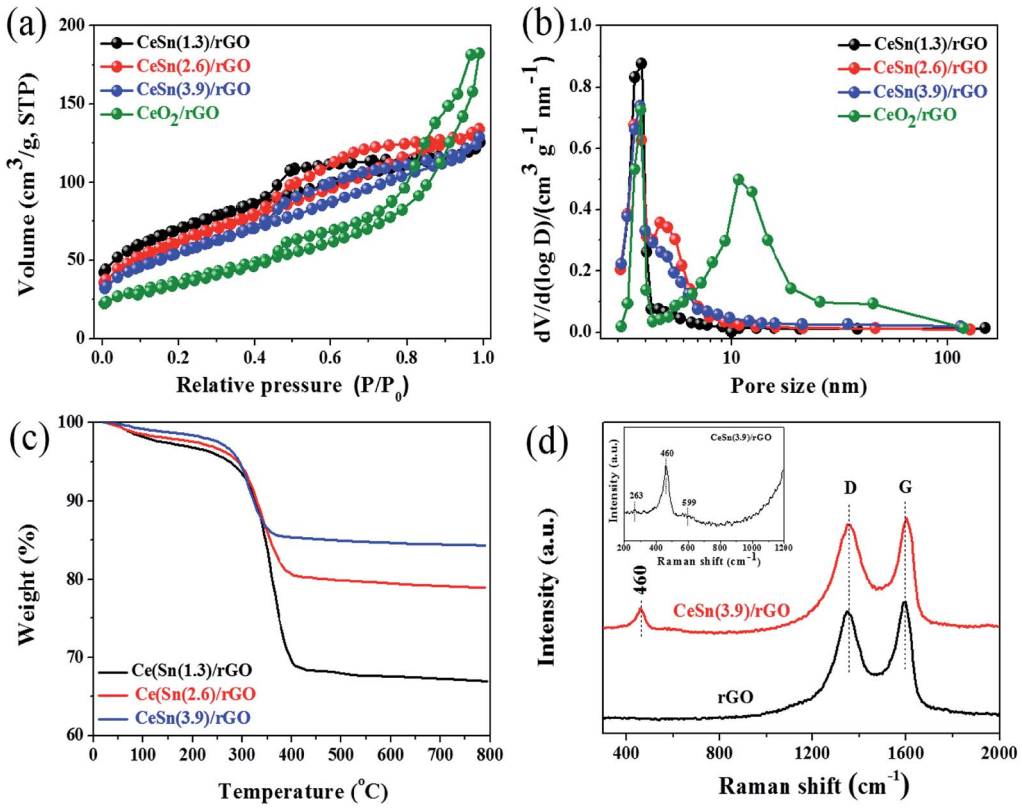

Fig. 4 (a) N_2 adsorption–desorption isotherms, (b) corresponding pore size distributions, (c) TG curves of the various catalysts, (d) Raman spectra of rGO and the CeSn(3.9)/rGO catalyst.

Table 1 Physical properties of various catalysts[a]

Sample	S_{BET} ($m^2\ g^{-1}$)	V_{total} ($cm^3\ g^{-1}$)	Average pore size (nm)	Lattice parameter[b] (Å)	Crystallize size[c] (nm)
CeO_2/rGO	133.4	0.28	8.43	5.419	13.3
CeSn(1.3)/rGO	249.1	0.19	3.29	5.361	3.7
Ce(Sn(2.6)/rGO	220.8	0.21	3.76	5.369	4.4
CeSn(3.9)/rGO	197.7	0.20	4.04	5.364	5.5

[a] S_{BET}: BET specific surface area; V_{total}: total pore volume. [b] Calculated from the diffraction peak of the (111) plane. [c] Calculated from the XRD peak of the (111) plane.

CeSn(3.9)/rGO, respectively, corresponding to the total contents of CeO_2 and SnO_x in the samples.

To analyze the chemical structure of CeSn(3.9)/rGO catalyst, the Raman spectroscopy is explored as shown in Fig. 4d. Two characteristic peaks at about 1350 (D band) and 1596 cm^{-1} (G band) can be clearly observed in both rGO and the CeSn(3.9)/rGO catalyst, corresponding to the sp^3 and sp^2 carbon atoms, respectively.[32] This phenomenon confirms the existence of rGO in the obtained sample. The ratio of relative intensity I_D/I_G reflects the degree of graphitization, defects and the domain size of graphitization. The I_D/I_G value of CeSn(3.9)/rGO catalyst (0.99) is higher than that of rGO (0.92), indicating much more defects in the CeSn(3.9)/rGO catalyst. Another peak at 460 cm^{-1} is also observed in the Raman spectrum of CeSn(3.9)/rGO catalyst, corresponding to the F_{2g} vibration mode of CeO_2 in the fluorite structure,[20,33] which indicates the presence of CeO_2 nanoparticles in the CeSn(3.9)/rGO catalyst. Unfortunately, the characteristic peaks at about 610 cm^{-1} corresponding to SnO_x cannot be observed,[34] suggesting that no pure SnO_x phase is formed. It is worth noting that two broad peaks at 263 and 599 cm^{-1} can be also observed in the CeSn(3.9)/rGO catalyst (the inset in Fig. 4d), which are related to the existence of oxygen vacancies.[35] The generation of oxygen vacancies could increases the oxygen storage capacity and transfer ability between Ce^{3+} and Ce^{4+}, which contributes to enhancing the SCR activity.[36]

The XRD patterns of the CeO_2–SnO_x/rGO catalysts with different mass ratios of (Ce + Sn)/GO were characterized, along with that of CeO_2/rGO for comparison (Fig. 5a). CeO_2/rGO catalyst shows characteristic diffraction peaks located at 28.5°, 33.1°, 47.5° and 56.4°, which can be assigned to (111), (200), (220) and (311) planes of cubic CeO_2 crystalline (JCPDS card no. 34-0394), respectively.[37,38] For CeO_2–SnO_x/rGO catalysts, only diffraction peaks of cubic CeO_2 are observed and the typical characteristic peaks of SnO_2 located at 26.7°, 33.9° and 51.6° can not be observed,[39,40] in accordance with TEM and Raman results, indicating the replacement of Ce^{4+} by Sn^{4+} due to the smaller ionic radius of Sn^{4+} than Ce^{4+}(the former is 0.069 nm, the latter is 0.087 nm). Meanwhile, no a broad peak around 26° related to the restacked rGO is detected, suggesting the as-prepared grapheme oxide is well exfoliated. It is worth pointing out that the diffraction peaks of CeO_2–SnO_x/rGO catalysts slightly shift to higher angle compared to those of CeO_2/rGO catalyst. This result further suggests Sn^{4+} can be incorporated into the lattice of CeO_2 to form the CeO_2–SnO_x solid solution. Such catalyst solid solution phenomenonon was also reported by Chen *et al.* on CuO/$Ce_xSn_{1-x}O_2$ catalysts ($1 - x \leq 0.2$), which found the formation of homogeneous solid solutions between CeO_2 and SnO_2.[41] Similar explanations were also elucidated by Machida *et al.* on MnO_x–CeO_2 binary oxides, where the replacement of Ce^{4+} by Mn^{3+} in the fluorite structure results in the formation of a solid solution between Mn_2O_3 and CeO_2.[16,42] Additionally, CeO_2 diffraction peaks of CeO_2–SnO_x/rGO catalysts are broader than those of individual CeO_2/rGO and the crystallize size of CeO_2–SnO_x/rGO catalysts is smaller than that of CeO_2/rGO (Table 1), further confirming the formation of CeO_2–SnO_x solid solution resulted from the interaction between cerium and tin species, which leads to higher dispersion of the metal oxides on the surface of CeO_2–SnO_x/rGO. Therefore, the improved dispersion of cerium and tin species on the catalyst surface plays a positive effect on SCR activity, which is consistent with SCR activity results.

To illustrate the different types of chemical functional groups in the obtained samples from GO to the CeSn(3.9)/rGO catalyst, FT-IR spectra were carried out. As shown in Fig. 5b, the representative absorption peaks ofGO can be observed, including the stretching vibration peak of O–H group at approximately 3420 cm^{-1}, the C=O (COOH) stretching vibration peak at 1720 cm^{-1}, the aromatic C=C stretching vibration peak at approximately 1624 cm^{-1}, the C–OH deformation vibration peak at 1407 cm^{-1}, and the alkoxy C–O stretching vibration peak at 1080 cm^{-1}.[43,44] For the CeSn(3.9)/rGO catalyst, the spectrum peaks of C=O, C–OH and C–O are significantly weakened. This result further confirms GO is reduced to rGO during the hydrothermal treatment, agreeing well with the Raman result.

To further determine the chemical composition of the CeO_2–SnO_x/rGO catalyst, the XPS analysis was performed. Fig. 6 presents the XPS survey spectra of CeSn(1.3)/rGO and CeSn(3.9)/rGO, revealing the presence characteristic peaks of cerium, tin, carbon and oxygen. And the detail surface atomic concentrations of Ce, Sn, C, O and the relative atomic ratios of $Ce^{3+}/(Ce^{3+} + Ce^{4+})$ are summarized in Table 2. Fig. 7a shows the XPS spectra of C 1s. Three peak at 284.8, 286.6 and 289.0 eV are observed, corresponding to the C–C, the C–O, and O–C=O groups,

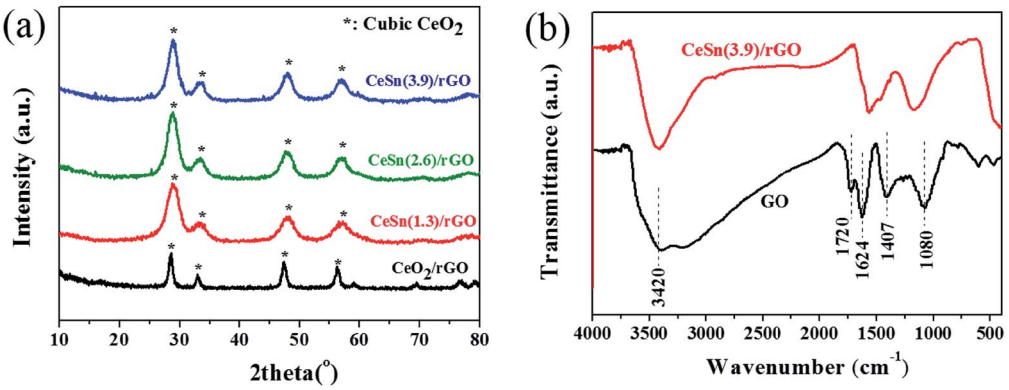

Fig. 5 (a) XRD patterns of the various catalysts. (b) FT-IR spectra of GO and the CeSn(3.9)/rGO catalyst.

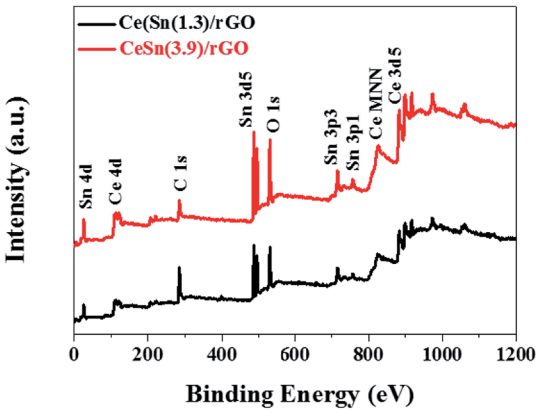

Fig. 6 XPS survey spectra of the different catalysts.

Table 2 XPS results of the different catalysts

	Surface atomic concentration (%)					Atomic ratio (%)
				O		
Sample	Ce	Sn	C	O_α	O_β	$Ce^{3+}/(Ce^{3+} + Ce^{4+})$
CeSn(1.3)/rGO	2.80	4.09	64.87	18.33	9.92	18.7
CeSn(3.9)/rGO	5.59	7.59	40.12	33.13	13.57	19.8

respectively.[45] The low intensities of C–O, and O–C=O functional groups in the obtained samples indicate the reduction of GO to rGO during the hydrothermal process,[46] which is consistent with the Raman and FT-IR results.

The O 1s XPS spectra are fitted into two peaks and the results are shown in Fig. 7b. Two peaks at 529.5–530.2 eV and 531.2–532.0 eV correspond to the peaks of lattice oxygen (O_α) and chemisorbed oxygen (O_β), respectively.[37] As shown in Fig. 7b and Table 2, the O_α concentration of CeSn(3.9)/rGO markly increases compared with that of CeSn(1.3)/rGO, due to increased lattice oxygen in SnO_x and CeO_2 with the increasing of (Ce + Sn)/GO mass ratio. It is worth noting that the O_β concentration on CeSn(3.9)/rGO (13.57%) is higher than that on CeSn(1.3)/rGO (9.92%), indicating increased chemisorbed oxygen concentration on the surface of CeSn(3.9)/rGO. It has been generally accepted that the chemisorbed oxygen species (O_β) are more active than the lattice oxygen species (O_α) due to their higher oxygen mobility.[47] Furthermore, the higher concentration of O_β is beneficial for the oxidation of NO to NO_2, which accelerates the "fast SCR" process ($4NH_3 + 2NO + 2NO_2 \rightarrow 4N_2 + 6H_2O$) and hence promotes the catalytic activity.[48]

The Ce 3d XPS spectra are shown in Fig. 7c. The u‴, u″, u, v‴, v″, and v peaks are assigned to Ce^{4+}, while the peaks labeled u′ and v′ are attributed to Ce^{3+}.[37,49] For the two catalysts, the intensities of the u′ and v′ peaks for $Ce^{3+}$are much weaker than those of the u‴, u″, u, v‴, v″, and v peaks for Ce^{4+}, suggesting that Ce^{4+} and Ce^3 coexist and the main valence state of cerium is Ce^{4+}. It is noted that the intensities of Ce^{4+} and Ce^{3+} peaks in CeSn(3.9)/rGO are much stronger than those in CeSn(1.3)/rGO, indicating increased concentrations of Ce^{4+} and Ce^{3+}. The ratios of $Ce^{3+}/(Ce^{3+} + Ce^{4+})$ can be determined by the area ratio of Ce^{3+} species. As illustrated by Table 2, the ratio of $Ce^{3+}/(Ce^{3+} + Ce^{4+})$ in CeSn(3.9)/rGO (19.8%) is slightly higher than that in CeSn(1.3)/rGO (18.7%). It has been reported that the existence

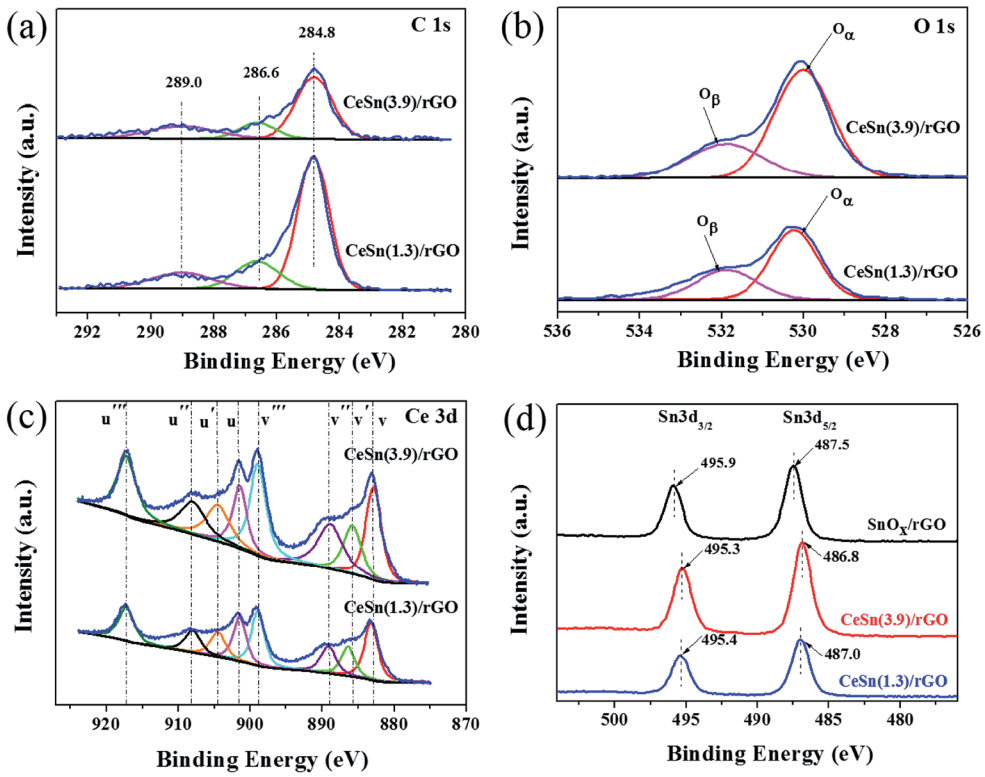

Fig. 7 XPS spectra of C 1s (a), O 1s (b), Ce 3d (c) and Sn 3d (d) for the different catalysts.

of Ce^{3+} can create charge imbalance to form oxygen vacancies and unsaturated chemical bonds,[26,50] leading to the increase in chemisorbed oxygen on the catalyst surface, in accordance with the above results of O 1 s spectra. Thus, the higher ratio of $Ce^{3+}/(Ce^{3+} + Ce^{4+})$ in CeSn(3.9)/rGO implies the generation of more oxygen vacancies. The increase of oxygen vacancies on the catalyst surface could result in more gaseous oxygen being supplied on the catalyst.[51] Moreover, higher concentration of oxygen vacancies is advantageous to the improvement of oxygen mobility.[52] Both of them could facilitate the activation and transportation of the active oxygen species in the SCR reactions, which result in the excellent SCR activity of CeSn(3.9)/rGO catalyst, as evidenced by the results shown in Fig. 2a.

Fig. 7d presents the Sn 3d XPS spectra of SnO_x/rGO, CeSn(1.3)/rGO and CeSn(3.9)/rGO. The binding energies of Sn $3d_{3/2}$ and Sn $3d_{5/2}$ in SnO_x/rGO are located at 495.9 and 487.5 eV, respectively, indicating the existence of Sn^{4+}.[21,40] Compared with SnO_x/rGO, the peaks of Sn $3d_{3/2}$ and Sn $3d_{5/2}$ in CeSn(1.3)/rGO and CeSn(3.9)/rGO catalysts slightly shift to lower binding energies. The shift in binding energy indicates that there are excess electrons around Sn atoms on CeSn(1.3)/rGO and CeSn(3.9)/rGO, and the existence of synergistic interaction between cerium and tin oxides is further demonstrated by the following redox equilibrium: $Sn^{4+} + 2Ce^{3+} \leftrightarrow Sn^{2+} + 2Ce^{4+}$.[53] The above XPS results demonstrate that relatively high concentrations of chemisorbed oxygen species, oxygen vacancies and $Ce^{3+}/(Ce^{3+} + Ce^{4+})$ are beneficial for the SCR activity of CeSn(3.9)/rGO catalyst.

3.3 NH_3-TPD analysis

It is generally recognized that the adsorption and activation (partial oxidation: $NH_{3(ads)} \rightarrow NH_{2(ads)}$) of NH_3 is a key step in the NH_3-SCR reaction.[54,55] Therefore, the adsorption and activation of NH_3 is promoted by increasing the surface acidity of the catalyst, which is favorable for improving SCR activity. NH_3-TPD experiments were carried out to measure the acidity of the obtained catalysts. Fig. 8 shows the NH_3-TPD curves for CeO_2/rGO, CeSn(1.3)/rGO and CeSn(3.9)/rGO. For CeO_2/rGO, one desorption peak appeared at 150–320 °C is assigned to the weak acid sites, while another broad desorption peak at 350–620 °C is assigned to the strong acid sites. For CeSn(1.3)/rGO and CeSn(3.9)/rGO, two obvious desorption peaks above 350 °C are observed. It is widely accepted that the position of NH_3 desorption peak is connected with the acid strength and the area of desorption peak is proportional to the acid amount. Compared with CeO_2/rGO, the desorption peaks of CeSn(1.3)/rGO and CeSn(3.9)/rGO markly shift to higher temperature, suggesting that the strength of strong acid sites become stronger after the addition of SnO_x. Meanwhile, the desorption peak areas of CeSn(1.3)/rGO and CeSn(3.9)/rGO are larger than that of CeO_2/rGO, indicating that there are more strong acid sites on them. It could be attributed to the larger specific surface area of CeSn(1.3)/rGO and CeSn(3.9)/rGO (Table 1). The amount of strong acid sites on CeSn(3.9)/rGO is lower than that of CeSn(1.3)/rGO, probably due to the decrease in specific surface area (Table 1). Additionally, the desorption peak temperature of CeSn(3.9)/rGO is higher than that of CeSn(1.3)/rGO, suggesting that the strength of strong acid sites on CeSn(3.9)/rGO is stronger. The stronger acid sites could be related to the stronger interaction between CeO_2 and SnO_x on CeSn(3.9)/rGO. Therefore, CeSn(3.9)/rGO has more amount and stronger strength of strong acid sites, which facilitates the adsorption and activation of NH_3, resulting in the higher SCR activity of CeSn(3.9)/rGO.

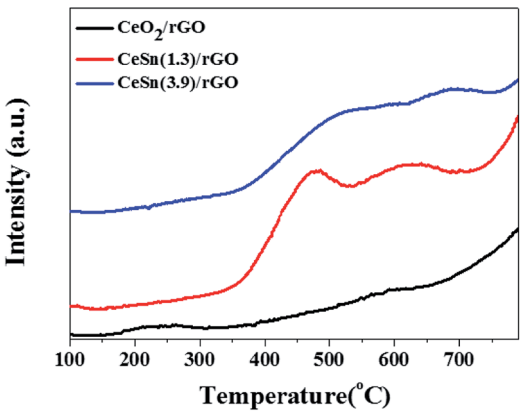

Fig. 8 NH_3-TPD profiles of the various catalysts.

3.4 Effect of SO_2 on SCR activity

The actual flue gas still contains some residual SO_2 even after desulfurization, and thus it is necessary to investigate the SO_2 resistance of CeSn(3.9)/rGO catalyst in the temperature range of 120–280 °C. Fig. 9 presents the effect of SO_2 on SCR activity of CeSn(3.9)/rGO catalyst at 240 °C. After the introduction of 200 ppm SO_2 into the feed stream, NO conversion gradually decreases from about 95% to about 63% in 180 min. After SO_2 is shut off, NO conversion cannot be recovered to the original value, but NO conversion still maintains at about 65%. Such results suggest that CeSn(3.9)/rGO catalyst has a certain SO_2 resistance. Since CeSn(3.9)/rGO catalyst not only exhibits high SCR activity in the temperature range of 120–280 °C but also presents good SO_2 resistance, CeSn(3.9)/rGO catalyst seems to have promising prospect for NO removal at low temperature.

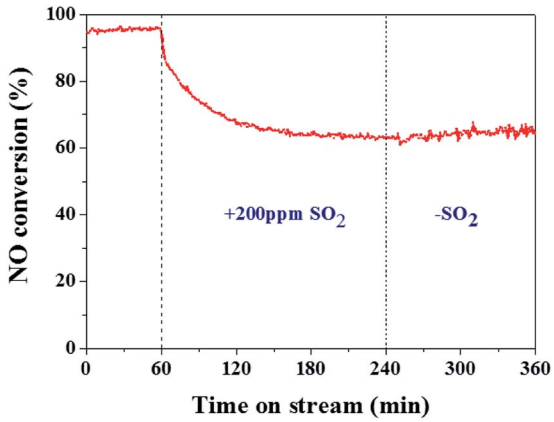

Fig. 9 Effect of SO_2 on SCR activity of CeSn(3.9)/rGO catalyst at 240 °C.

4. Conclusions

The CeO_2–SnO_x anchored on reduced graphene oxide (CeO_2–SnO_x/rGO) catalysts were successfully synthesized using hydrothermal method. The CeO_2–SnO_x/rGO catalysts show high SCR activities in the temperature range of 120–280 °C. About 86% NO conversion at 160 °C and more than 97% NO conversion in the temperature range of 200–280 °C are achieved over the CeSn(3.9)/rGO catalyst. All the catalysts yield higher than 95% N_2 selectivity at 120–280 °C. Additionally, CeSn(3.9)/rGO catalyst presents a certain SO_2 resistance. The excellent SCR activity can be attributed to the highly dispersed CeO_2 nanoparticles on the rGO nanosheets, and its mesoporous structures with large specific surface area. More importantly, there are higher ratio of $Ce^{3+}/(Ce^{3+} + Ce^{4+})$, higher concentrations of surface chemisorbed oxygen and oxygen vacancies, more amount of strong acid sites and stronger acid strength on the surface of CeSn(3.9)/rGO catalyst, because there exists the synergistic interaction between cerium and tin oxides. These factors contribute to higher SCR activity of CeSn(3.9)/rGO catalyst. Further experiments are underway to elucidate the mechanisms of SO_2 deactivation and SCR reaction over CeO_2–SnO_x/rGO catalyst.

Conflicts of interest

There are no conflicts to declare.

Acknowledgements

This work was financially supported by National Science Foundation of China (No. 51472086, 51002051, 20806024) and CAS Key Laboratory of Carbon Materials (No. KLCMKFJJ1703).

References

1 G. Busca, L. Lietti, G. Ramis and F. Berti, *Appl. Catal., B*, 1998, **18**, 1–36.
2 H. Bosch and F. Janssen, *Catal. Today*, 1988, **2**, 369–379.
3 P. Forzatti, *Catal. Today*, 2000, **62**, 51–65.
4 M. D. Amiridis, I. E. Wachs, G. Deo, J. M. Jehng and D. S. Kim, *J. Catal.*, 1996, **161**, 247–253.
5 B. Q. Jiang, Y. Liu and Z. B. Wu, *J. Hazard. Mater.*, 2009, **162**, 1249–1254.
6 Z. B. Wu, R. B. Jin, Y. Liu and H. Q. Wang, *Catal. Commun.*, 2008, **9**, 2217–2220.
7 W. Q. Xu, Y. B. Yu, C. B. Zhang and H. He, *Catal. Commun.*, 2008, **9**, 1453–1457.
8 Z. G. Huang, Z. P. Zhu and Z. Y. Liu, *Appl. Catal., B*, 2002, **39**, 361–368.
9 B. X. Shen and T. Liu, *Acta Phys.-Chim. Sin.*, 2010, **26**, 3009–3016.
10 X. Wang, Y. Y. Zheng, Z. Xu, Y. Liu and X. L. Wang, *Catal. Sci. Technol.*, 2014, **4**, 1738–1741.
11 L. Zhang, D. S. Zhang, J. P. Zhang, S. X. Cai, C. Fang, L. Huang, H. R. Li, R. H. Gao and L. Y. Shi, *Nanoscale*, 2013, **5**, 9821–9829.
12 S. X. Cai, H. Hu, H. R. Li, L. Y. Shi and D. S. Zhang, *Nanoscale*, 2016, **8**, 3588–3598.
13 Y. L. Wang, Z. Y. Liu, L. Zhan, Z. G. Huang, Q. Y. Liu and J. R. Ma, *Chem. Eng. Sci.*, 2004, **59**, 5283–5290.
14 Y. L. Wang, X. X. Li, L. Zhan, C. Li, W. M. Qiao and L. C. Ling, *Ind. Eng. Chem. Res.*, 2015, **54**, 2274–2278.
15 Z. M. Liu, Y. Yi, S. X. Zhang, T. L. Zhu, J. Z. ZhuandJ and G. Wang, *Catal. Today*, 2013, **216**, 76–81.
16 G. Qi, R. T. Yang and R. Chang, *Appl. Catal., B*, 2004, **51**, 93–106.
17 B. M. Reddy, A. Khan, Y. Yamada, T. Kobayashi, S. Loridant and J. C. Volta, *J. Phys. Chem. B*, 2003, **107**, 5162–5167.
18 A. Trovarelli, F. Zamar, J. Llorca, C. deLeitenburg, G. Dolcetti and J. T. Kiss, *J. Catal.*, 1997, **169**, 490–502.
19 H. Z. Chang, J. H. Li, X. Y. Chen, L. Ma, S. J. Yang, J. W. Schwank and J. M. Hao, *Catal. Commun.*, 2012, **27**, 54–57.
20 H. Z. Chang, X. Y. Chen, J. H. Li, L. Ma, C. Z. Wang, C. X. Liu, J. W. Schwank and J. M. Hao, *Environ. Sci. Technol.*, 2013, **47**, 5294–5301.
21 Y. L. Wang, Z. G. He, L. Zhan and M. Ge, *New Carbon Mater.*, 2015, **30**, 533–538.
22 Z. M. Liu, X. Feng, Z. Z. Zhou, Y. J. Feng and J. H. Li, *Appl. Surf. Sci.*, 2018, **428**, 526–533.
23 A. V. Murugan, T. Muraliganth and A. Manthiram, *Chem. Mater.*, 2009, **21**, 5004–5006.
24 S. F. Pei and H. M. Cheng, *Carbon*, 2012, **50**, 3210–3228.
25 W. S. Hummers and R. E. Offeman, Preparation of graphitic oxide, *J. Am. Chem. Soc.*, 1958, **80**, 1339.
26 M. E. Yu, C. T. Li, G. M. Zeng, Y. Zhou, X. N. Zhang and Y. E. Xie, *Appl. Surf. Sci.*, 2015, **342**, 174–182.
27 P. Li, Q. Y. Liu and Z. Y. Liu, *Ind. Eng. Chem. Res.*, 2011, **50**, 1906–1910.
28 L. Zhang, L. L. Li, Y. Cao, Y. Xiong, S. G. Wu, J. F. Sun, C. J. Tang, F. Gao and L. Dong, *Catal. Sci. Technol.*, 2015, **5**, 2188–2196.
29 G. D. Zhang, We. L. Han, H. J. Zhao, L. Y. Zong and Z. C. Tang, *Appl. Catal., B*, 2018, **226**, 117–126.
30 Q. C. Lin, J. H. Li, L. Ma and J. M. Hao, *Catal. Today*, 2010, **151**, 251–256.
31 J. F. Liang, Y. K. Liu, L. Guo and L. D. Li, *RSC Adv.*, 2013, **3**, 11489–11492.
32 K. N. Kudin, B. Ozbas, H. C. Schniepp, R. K. Prud'homme, I. A. Aksay and R. Car, *Nano Lett.*, 2008, **8**, 36–41.
33 D. Y. Deng, N. Chen, X. C. Xiao, S. F. Du and Y. D. Wang, *Ionics*, 2017, **23**, 121–129.
34 L. Abello, B. Bochu, A. Gaskov, S. Koudryavtseva, G. Lucazeau and M. Roumyantseva, *J. Solid State Chem.*, 1998, **135**, 78–85.
35 Y. X. Gao, R. T. Li, S. L. Chen, L. F. Luo, T. Cao and W. X. Huang, *Phys. Chem. Chem. Phys.*, 2015, **17**, 31862–31871.
36 Y. Xiong, C. J. Tang, X. J. Yao, L. Zhang, L. L. Li, X. B. Wang, Y. Deng, F. Gao and L. Dong, *Appl. Catal., A*, 2015, **495**, 206–216.
37 Y. L. Wang, C. Z. Ge, L. Zhan, C. Li, W. M. Qiao and L. C. Ling, *Ind. Eng. Chem. Res.*, 2012, **51**, 11667–11673.

38 M. Vanitha, Keerthi, P. Cao and N. Balasubramanian, *J. Alloys Compd.*, 2015, **644**, 534–544.
39 X. L. Li, Y. H. Li, S. S. Deng and T. A. Rong, *Catal. Commun.*, 2013, **40**, 47–50.
40 X. L. Xu, R. B. Zhang, X. R. Zeng, X. Han, Y. C. Li, Y. Liu and X. Wang, *ChemCatChem*, 2013, **5**, 2025–2036.
41 Y. Z. Chen, B. J. Liaw and H. C. Chen, *Int. J. Hydrogen Energy*, 2006, **31**, 427–435.
42 M. Machida, M. Uto, D. Kurogi and T. Kijima, *J. Mater. Chem.*, 2001, **11**, 900–904.
43 J. L. Zhang, H. J. Yang, G. X. Shen, P. Cheng, J. Y. Zhang and S. W. Guo, *Chem. Commun.*, 2010, **46**, 1112–1114.
44 H. M. Xu, Z. Qu, C. X. Zong, W. J. Huang, F. Q. Quan and N. Q. Yan, *Environ. Sci. Technol.*, 2015, **49**, 6823–6830.
45 I. Nam, N. D. Kim, G. P. Kim, J. Park and J. Yi, *J. Power Sources*, 2013, **244**, 56–62.
46 J. W. Lee, A. S. Hall, J. D. Kim and T. E. Mallouk, *Chem. Mater.*, 2012, **24**, 1158–1164.
47 W. P. Shan, F. D. Liu, H. He, X. Y. Shi and C. B. Zhang, *Catal. Today*, 2012, **184**, 160–165.
48 B. X. Shen, Y. Y. Wang, F. M. Wang and T. Liu, *Chem. Eng. J.*, 2014, **236**, 171–180.
49 T. T. Gu, Y. Liu, X. L. Weng, H. Q. Wang and Z. B. Wu, *Catal. Commun.*, 2010, **12**, 310–313.
50 S. X. Yang, W. P. Zhu, Z. P. Jiang, Z. X. Chen and J. B. Wang, *Appl. Surf. Sci.*, 2006, **252**, 8499–8505.
51 Q. Shen, L. Y. Zhang, N. N. Sun, H. Wang, L. S. Zhong, C. He, W. Wei and Y. H. Sun, *Chem. Eng. J.*, 2017, **322**, 46–55.
52 B. Guan, H. Lin, L. Zhu and Z. Huang, *J. Phys. Chem. C*, 2011, **115**, 12850–12863.
53 X. J. Yao, Y. Xiong, W. X. Zou, L. Zhang, S. G. Wu, X. Dong, F. Gao, Y. Deng, C. J. Tang, Z. Chen, L. Dong and Y. Chen, *Appl. Catal., B*, 2014, **144**, 152–165.
54 G. Ramis, Y. Li, G. Busca, M. Turco, E. Kotur and R. J. Willey, *J. Catal.*, 1995, **157**, 523–535.
55 G. Ramis, Y. Li and G. Busca, *Catal. Today*, 1996, **28**, 373–380.